Journal of Advanced Ceramics
2024, **13**(3): 345–353
https://doi.org/10.26599/JAC.2024.9220859

Research Article

Excellent energy storage performance in $Bi_{0.5}Na_{0.5}TiO_3$-based lead-free high-entropy relaxor ferroelectrics via B-site modification

Kaihua Yang[1,†], Gengguang Luo[1,†], Li Ma[1], Ruoxuan Che[1], Zhiyi Che[1], Qin Feng[1,✉], Zhenyong Cen[1], Xiyong Chen[1], Jiajun Zhou[2,✉], Nengneng Luo[1,✉]

[1] *State Key Laboratory of Featured Metal Materials and Life-cycle Safety for Composite Structures, School of Resources, Environment and Materials, Guangxi University, Nanning 530004, China*
[2] *School of Optical and Electronic Information, Key Lab of Functional Materials for Electronic Information (B) of Ministry of Education, Huazhong University of Science and Technology, Wuhan 430074, China*

Received: November 23, 2023; Revised: January 24, 2024; Accepted: January 28, 2024

Abstract: Next-generation advanced high/pulsed power capacitors urgently require dielectric materials with outstanding energy storage performance. $Bi_{0.5}Na_{0.5}TiO_3$-based lead-free materials exhibit high polarization, but the high remanent polarization and large polarization hysteresis limit their applications in dielectric capacitors. Herein, high-entropy perovskite relaxor ferroelectrics $(Na_{0.2}Bi_{0.2}Ba_{0.2}Sr_{0.2}Ca_{0.2})(Ti_{1-x\%}Zr_{x\%})O_3$ are designed by adding multiple ions in the A-site and replacing the B-site Ti^{4+} with a certain amount of Zr^{4+}. The newly designed system showed high relaxor feature and slim polarization–electric (*P*–*E*) loops. Especially, improved relaxor feature and obviously delayed polarization saturation were found with the increasing of Zr^{4+}. Of particular importance is that both high recoverable energy storage density of 6.6 J/cm^3 and energy efficiency of 93.5% were achieved under 550 kV/cm for the ceramics of x = 6, accompanying with excellent frequency stability, appreciable thermal stability, and prosperous discharge property. This work not only provides potential dielectric materials for energy storage applications, but also offers an effective strategy to obtain dielectric ceramics with ultrahigh comprehensive energy storage performance to meet the demanding requirements of advanced energy storage applications.

Keywords: $(Bi_{0.5}Na_{0.5})TiO_3$; high-entropy perovskite ceramics; relaxor ferroelectrics (RFEs); polarization saturation; energy storage density

1 Introduction

Owing to charming characteristics such as ultra-high power density, swift charge–discharge speed, long lifespan, and excellent thermal stability, ceramic dielectric capacitors have been widely utilized in numerous advanced high/pulsed power electronic systems [1–3]. Nevertheless, their storage density is unable to meet the great requirement of miniaturization and integration [4]. Generally, the energy storage performance of a dielectric capacitor is evaluated by the recoverable energy-storage density (W_{rec}) and energy storage efficiency (η), which can be calculated from the integral of polarization–electric (*P*–*E*) field loop by Eqs. (1)–(3):

$$W_{tot} = \int_0^{P_m} E\mathrm{d}P \tag{1}$$

$$W_{rec} = \int_{Pr}^{P_m} E\mathrm{d}P \tag{2}$$

$$\eta = \frac{W_{rec}}{W_{tot}} \times 100\% \tag{3}$$

where W_{tot} is total energy storage density, P_m is the saturated polarization, P_r is the remanent polarization, and E is the applied electric field [5,6]. Based on the above equations, it can be deduced that the high energy storage density requires high breakdown strength (E_b), large P_m, and minimal P_r.

Relaxor ferroelectrics (RFEs) exhibit a slim hysteresis loop with large P_m and near-zero P_r due to the existence of polar nanoregions (PNRs), making them possess both high W_{rec} and η [7,8]. Generally, PNRs can be obtained by breaking long-range ordered domains in ferroelectrics (FEs), experimentally realized by doping heterogeneous ions to cause local compositional inhomogeneity and ion disorder [9,10]. Based on this consideration, a large amount of $BaTiO_3$- and $(Bi_{0.5}Na_{0.5})TiO_3$-based RFE materials has been developed, such as $BaTiO_3$–$CaZrO_3$ [11], $BaTiO_3$–$Bi(Mg_{2/3}Nb_{1/3})O_3$ [12], $(Bi_{0.5}Na_{0.5})TiO_3$–$BaTiO_3$ [13], $(Bi_{0.5}Na_{0.5})TiO_3$–$SrTiO_3$ [14], $(Bi_{0.5}Na_{0.5})TiO_3$–$AgNb_{0.5}Ta_{0.5}O_3$ [15], and $(Bi_{0.5}Na_{0.5})TiO_3$–$NaNbO_3$ [16], which greatly optimized energy storage performance. However, the above relaxor systems are hard to further improve the ion disorder by chemical doping due to the Gibbs phase rule, which leads to the restriction of relaxor feature [17,18].

Recently, "high-entropy ceramics" (HECs), which consist of five or more ionic oxides that are mixed in a near equiatomic

† Kaihua Yang and Gengguang Luo contributed equally to this work.
✉ Corresponding authors.
E-mail: Q. Feng, fengqin307@163.com;
J. Zhou, jiajun612@sina.com;
N. Luo, luonn1234@163.com

ratio, have received great attention due to their unique composition, structure, and potential electrical properties [19]. In HECs, due to the existence of an ordered sub-lattice, the differentiation between cation lattice sites is small since each has the same immediate surroundings [20]. Therefore, a large number of quasi-equivalent sites in a crystal with an intermediate sub-lattice will increase the distribution homogeneousness of cations [21]. Of particular importance is that, random distributed multi-elements result in compositional disorder that reduces short-range order. Thus, it is easier to form isolated polar nanoclusters rather than long-range ordered domains in a dielectric HECs matrix. This characteristic makes it more likely to obtain a high relaxor feature and benefit for good energy storage performance [10,22]. This has been experimentally confirmed in some $(K,Na)NbO_3$-[23], $Bi_4Ti_3O_{12}$- [24] based ferroelectrics, in which highly disorder distributed ions were observed, which showed great slimmer *P*–*E* loops, significantly improved energy storage density, and efficiency.

$Bi_{0.5}Na_{0.5}TiO_3$ possesses high spontaneous polarization, which makes it promising for energy storage applications, but the large remanent polarization and hysteresis restrict its usage. By deliberately doping multiple ions (Ba^{2+}, Sr^{2+}, Ca^{2+}) with different ionic radii and valence states in the A site and forming homogeneous solid solution, new high-entropy ceramics, $(Na_{0.2}Bi_{0.2}Ba_{0.2}Sr_{0.2}Ca_{0.2})TiO_3$ (NBBSCT), were developed [25]. Due to the random distribution of different ions, the local compositional disorder occurs and generates PNRs. Nevertheless, the polarization still tends to saturate at the electric field far prior to their respective dielectric breakdown strength, due to the fast growth of PNRs to form micro-domains, as shown in Fig. 1. This feature restricts its further improvement in energy storage density, despite the high energy storage efficiency. That is to say, delaying the polarization saturation is of particular importance for improving the energy storage properties in the NBBSCT system.

It should be noticed that the local compositional disorder and PNRs of NBBSCT system are mainly caused by the alivolance A-site ions. In fact, the B-site ions also contribute to the relaxor feature in a ferroelectric system [23]. On the basis of the A-site disorder, an additional B-site disorder may further break the size of PNRs and weaken the coupling between PNRs. The highly broken and weak coupled PNRs may restrict their growth into micro-domains under high electric fields, thereby leading to slimmer *P*–*E* loops and further prolonged polarization saturation, as shown in Fig. 1.

It is reported that zirconium (Zr) is one of the most explored isovalent substitutions for titanium (Ti). Zhu *et al.* [26] indicated that Zr^{4+} modified $(Bi_{0.5}Na_{0.5})TiO_3$-based ceramics exhibited superior energy storage properties, owing to the optimization of E_b and delaying of polarization saturation. Meanwhile, the substitution of Ti^{4+} with Zr^{4+} is also an effective modification method in the perovskite ferroelectric ceramic system to promote the generation of PNRs [27]. Based on the above discussion, Zr^{4+} was selected to introduce into NBBSCT ceramics to further regulate relaxor properties and delay polarization saturation in this work. Encouragingly, the designed high-entropy ceramics exhibited high relaxor feature and significantly prolonged polarization saturation. Of particular importance is that the 6 mol% Zr^{4+} modified NBBSCT ceramics exhibited high W_{rec} of 6.6 J/cm^3 and ultra-high η of 93.5%. Our work proves that a B-site modification strategy on the basis of A-site high-entropy disorder is also an effective way of improving energy storage density.

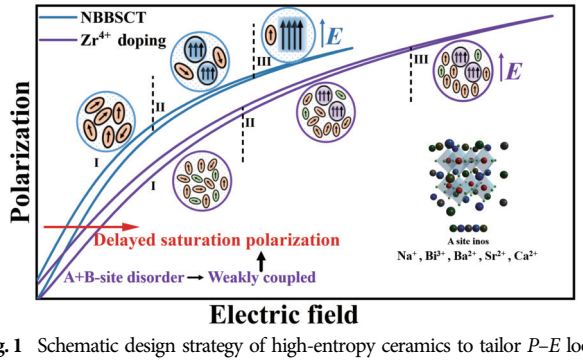

Fig. 1 Schematic design strategy of high-entropy ceramics to tailor *P*–*E* loops and associating changes of PNRs.

2 Experimental

$(Na_{0.2}Bi_{0.2}Ba_{0.2}Sr_{0.2}Ca_{0.2})(Ti_{1-x\%}Zr_{x\%})O_3$ (x = 0, 2, 4, 6, 8, 10, abbreviated as NBBSCT-xZ) ceramics, were synthesized by a conventional solid-state process. The raw materials were high-purity commercial powders of Na_2CO_3 (99.8%), Bi_2O_3 (99%), $BaCO_3$ (99%), $SrCO_3$ (99%), $CaCO_3$ (99%), TiO_2 (98%), and ZrO_2 (99.99%) (Sinopharm Chemical Reagent Co., Ltd., China). The powders were weighed based on stoichiometric ratio and then ball-milled for 12 h by 200 r/min. After drying, the mixed powders were calcined at 950–1000 ℃ for 4 h to get a pure phase. Then a second ball-milling for 12 h at 200 r/min was applied, after which the calcined powders were pressed into plates with a diameter of 8 mm and a thickness of ~1 mm, followed by further cold isostatic pressing under 300 MPa to improve density. The pellets were sintered at 1200–1250 ℃ for 4 h. For a dielectric measurement, the as-sintered pellets were polished into ~0.6 mm in thickness with both surfaces coated with silver electrodes. For ferroelectric and charge–discharge measurements, the thickness was polished to 0.10 mm with a silver electrode of 2.0 mm in diameter. The silver electrode was sintered at 600 ℃ for 30 min.

The phase structure of the NBBSCT-xZ ceramics was analyzed by an X-ray powder diffractometer (SmartLab-3 kW, Rigaku Ltd., Japan) with Cu Kα radiation. The temperature dependences of dielectric permittivity and dielectric losses were measured by a precision impendence analyzer (E4990A, Keysight, USA). The impedance spectra were tested by an electrochemical impedance spectroscope (1260AC and 1287AC, UK), connecting a muffle furnace with the test temperatures change from 625 to 725 ℃, and the test frequency ranged from 0.1 Hz to 1 MHz. The polarization versus electric field (*P*–*E*) hysteresis loops and current versus electric field (*I*–*E*) hysteresis loops were conducted by a ferroelectric tester (TF Analyzer 3000, aixACCT, Germany). The charge–discharge energy density was measured by a charge–discharge apparatus (PK-CPR1801–10015, Polyk Technology, USA). The selected-area electron diffractions were recorded through a transmission electron microscope (TEM; TECNAL G2 F30, FEI, USA).

3 Results and discussion

Figure 2(a) shows X-ray diffraction (XRD) patterns of NBBSCT-xZ ceramics, in which the peaks relevant to $K_{\alpha 2}$ ($K_{\alpha 2}$ ray is a kind of radiation generated when electrons move from the L layer to the K layer) are marked out. A typical perovskite structure can be detected for all samples, only a small amount of ZrO_2 comes out when x =10. This indicates the Zr^{4+} ions are well dissolved into the NBBSCT matrix till x =10. It should be noticed that the (110) peak gradually shifts to the low diffraction angles with the increase of the Zr^{4+} content, owing to the fact that Ti^{4+} (CN = 6, R_{Ti} = 0.605 Å) is substituted by Zr^{4+} (CN = 6, R_{Zr} = 0.72 Å) with larger ionic radii

[28] where R_{Ti} means the radii of Ti^{4+} and R_{Zr} means the radii of Zr^{4+}. To obtain the detailed lattice parameters, XRD Rietveld refinements were carried out by the GSAS software, as shown in Fig. 2(b) [15]. The Rietveld refinement results are listed in Table 1, and the lattice parameters (*a*, *b*, *c*) and volume (*V*) are drawn in Fig. 2(c). All compositions are well-constrained to the *P4bm* space group, indicating Zr^{4+} does not change the basic structure of NBBSCT. The lattice parameters and volume increase continuously with the addition of Zr^{4+}, as a result of its larger ionic radius.

To illustrate temperature-induced phase transition in NBBSCT-*x*Z ceramics, the temperature vs. dielectric permittivity (ε_r) and dielectric loss (tanδ) spectra are measured and shown in Figs. 3(a)–3(f). Obvious dielectric peaks (the corresponding temperature called as T_m) are observed in all samples, associated with remarkable peaks in dielectric loss, as the phase structure transforms from ferroelectric (FE) to paraelectric (PE) phases. All dielectric peaks show evident frequency dispersion, giving a sign of a relaxor feature. As the increase of the Zr^{4+} content, the dielectric peaks gradually broaden and are compressed, with T_m slightly shifting downward to room temperature (RT) (Figs. 3(g)–3(i)). In addition, ε_m shows a general decrease with the increase of the Zr^{4+} content (Fig. 3(i)), as a result of the lower electronic polarizability of Zr^{4+} compared to Ti^{4+} which reduces the sensitivity of response of Zr^{4+} to the electric field [29].

To further estimate the relaxation characteristic, the relaxor factor (γ) is calculated according to the reformed Curie–Weiss law (Eq. (A.1)) [30, 31]. The fitting lines are shown in Fig. 4(a), which shows good reliability. γ exhibits a slight increase from 1.77 for x = 0 to a maximal value of 1.85 for x = 10, indicating high and slightly improved diffuseness of the phase transition and relaxor behavior. This concept can be further consolidated by the frequency dispersion ($\Delta T = T_m$ (1 MHz) − T_m (1 kHz)) of T_m [31], which exhibits a large temperature span and slightly increases from ~41 ℃ for x = 0 to ~45 ℃ for x = 10, as shown in Fig. 4(b). It should be noticed that, even though an increase of γ and ΔT is observed after the Zr^{4+} modification, the variations are actually not significant for both. To further determine the effect of the Zr^{4+} content on diffuseness, the normalized dielectric permittivity ($\varepsilon_r/\varepsilon_m$) vs. temperature ($T$) curves are figured, as shown in Fig. 4(c). Herein, the parameters T_{R-L} and T_{R-H} (R = 1/2, 2/3; T_{R-L} and T_{R-H} represent the span between T_m and the temperature where $\varepsilon_r/\varepsilon_m$ is R of the maximum value from the low-temperature and the high-temperature branches of the peak, respectively) to describe the width of the FE–PE dielectric peak around T_m [32,33] as given in Fig. 4(c). Generally, larger T_{R-L} and T_{R-H} indicate a slower phase transition process and higher relaxor feature [33]. Both T_{R-L} and T_{R-H} broaden apparently with the increase of the Zr^{4+} content, as

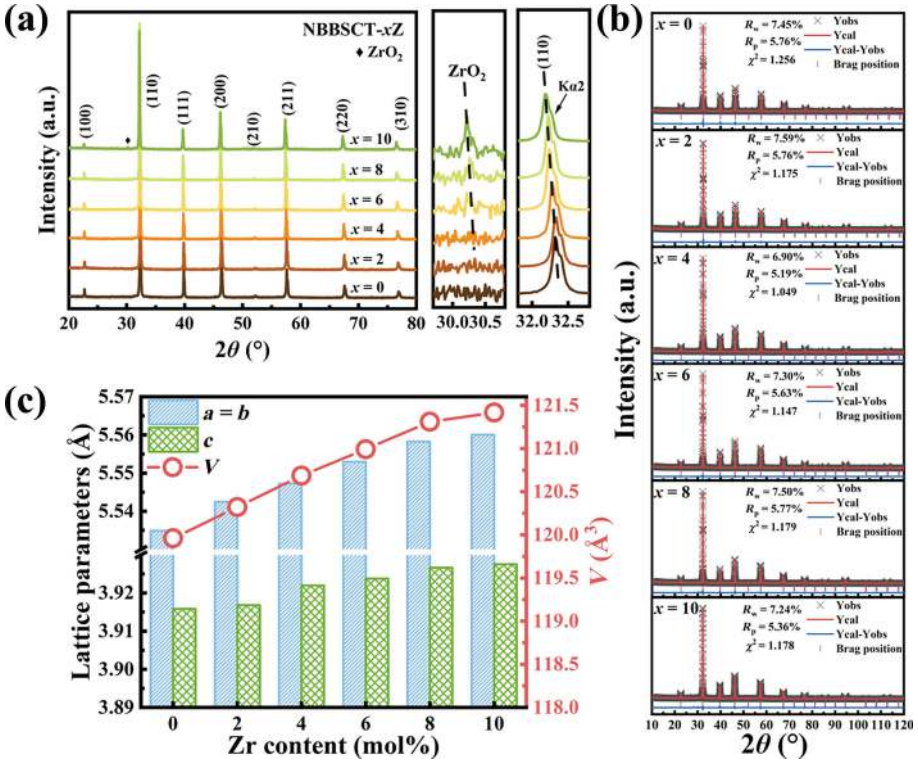

Fig. 2 (a) XRD pattern of NBBSCT-*x*Z ceramics at 2θ = 20°–80°. (b) Rietveld refinements of XRD data where R_{wp} is the reliability factors of weighted pattern, R_p is the reliability factors of pattern, and χ^2 is the goodness-of-fit indicator. (c) Lattice parameters (*a*, *b*, *c*), and lattice volume (*V*) derived from XRD Rietveld refinements.

Table 1 Refined structural parameters of NBBSCT-*x*Z ceramics

x	Space group	Lattice parameter (Å)	*V* (Å³)	R_{wp} (%)	R_p (%)	χ^2
0	*P4bm*	*a* = 5.5349, *b* = 5.5349, *c* = 3.9158	119.961	7.45	5.76	1.256
2	*P4bm*	*a* = 5.5425, *b* = 5.5425, *c* = 3.9168	120.321	7.59	5.76	1.175
4	*P4bm*	*a* = 5.5472, *b* = 5.5472, *c* = 3.9220	120.686	6.90	5.19	1.049
6	*P4bm*	*a* = 5.5530, *b* = 5.5530, *c* = 3.9238	120.992	7.30	5.63	1.147
8	*P4bm*	*a* = 5.5583, *b* = 5.5583, *c* = 3.9266	121.311	7.50	5.77	1.179
10	*P4bm*	*a* = 5.5601, *b* = 5.5601, *c* = 3.9275	121.417	7.24	5.36	1.178

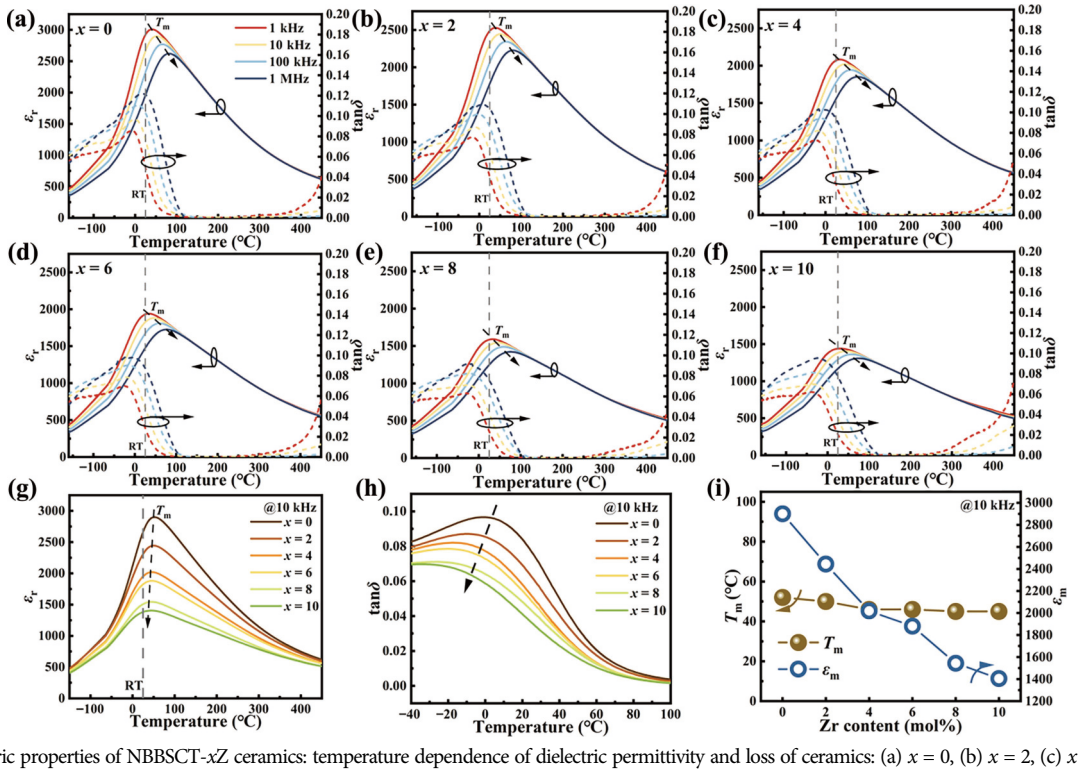

Fig. 3 Dielectric properties of NBBSCT-*x*Z ceramics: temperature dependence of dielectric permittivity and loss of ceramics: (a) $x = 0$, (b) $x = 2$, (c) $x = 4$, (d) $x = 6$, (e) $x = 8$, and (f) $x = 10$, where the solid lines respectively present dielectric permittivity while the dot lines present dielectric loss; (g) composition dependence of ε_r and tanδ; (h) composition dependence of tanδ from −40 to 100 ℃; (i) composition dependence of T_m and ε_m.

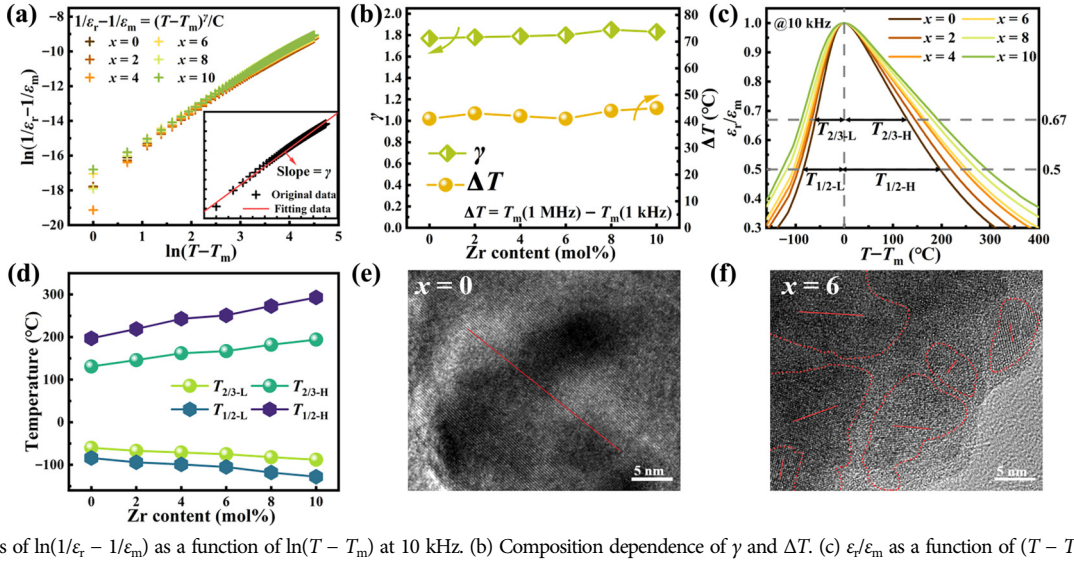

Fig. 4 (a) Plots of $\ln(1/\varepsilon_r - 1/\varepsilon_m)$ as a function of $\ln(T - T_m)$ at 10 kHz. (b) Composition dependence of γ and ΔT. (c) $\varepsilon_r/\varepsilon_m$ as a function of $(T - T_m)$ for different compositions at 10 kHz where the inset is expanded curves. (d) Composition dependent corresponding parameters $T_{R\text{-}L}$ and $T_{R\text{-}H}$ ($R = 1/2, 2/3$). TEM images taken from (e) NBBSCT and (f) NBBSCT-6Z ceramics.

shown in Fig. 4(d). This phenomenon, plus the change of γ and ΔT, gives an obvious sign that the zirconium additive actually contributes to the enhancement of the relaxor feature. In addition, Figs. 4(e) and 4(f) give TEM images of the ceramics of $x = 0$ and $x = 6$. The ceramics of $x = 0$ show an apparent parallel larger microregion, while the one of $x = 6$ exhibits the smaller nanoregions with diverse directions (see the red circles), revealing the high structural inhomogeneity at the nanoscale with the introduction of zirconium additive. This phenomenon indicates that the doping of Zr^{4+} could further reduce the domain size, which is in favor of enhanced relaxor properties of the ceramics. The strong relaxor feature hinders PNRs from forming long-range ferroelectric domains under an electric field and enables the domains easier switch back to the original state, which may delay the polarization saturation and result in a slim *P*–*E* loop, thereby leading to high energy storage density and efficiency.

The energy storage density is closely associated with high breakdown strength. To evaluate the value of the breakdown strength, Weibull distribution is adopted to analyze the data obtained by breakdown measurement at room temperature. Based on Eqs. (A.2.1) and (A.2.2) in the Appendix [34], Weibull distribution is fitted and shown in Fig. 5(a). E_b increases from 408 kV/cm for $x = 0$ and reaches a maximum of 513 kV/cm for $x = 6$, which exhibits a tendency to decrease by further increasing the

Zr^{4+} content, as shown in Fig. 5(b). To explore the inner mechanism of the effect of Zr^{4+} on the breakdown strength, the room-temperature electrical resistivity (ρ) is measured as a function of the Zr^{4+} content, as displayed in Fig. 5(c). All samples exhibit high electrical resistivity, indicating good electrical insulation properties. It is interesting that ρ increases first and then decreases with the increasing amount of Zr^{4+}, which reaches a maximum at $x = 6$. The high-temperature complex impedance spectra also exhibit a similar tendency to the room temperature electrical resistivity, in which the radius of a semicircle arc increases first and then decreases after Zr^{4+} doping, as shown in Fig. 5(d). Also, the complex impedance tested results at other temperatures are shown in Fig. S1 in the Electronic Supplementary Material (ESM), in which the radius of the semicircle arc decreases with increasing the temperature. After Arrhenius fitting (Fig. 5(e)), the electrical conductivity activation energy (E_a) is obtained and presented in Fig. 5(f). The calculated E_a is around 1.85–1.98 eV with the change of the Zr^{4+} content, revealing an oxygen vacancy-controlled conducting mechanism (0.5 eV ≤ E_a ≤ 2.0 eV) in the measuring temperature range [35–37]. Analogous to the change of electrical resistivity, E_a increases first with the addition of Zr^{4+} and then declines at a high Zr^{4+} level, reaching a maximum at $x = 6$. Larger E_a means a higher barrier for the migration/hopping of oxygen vacancies, which contributes to good electrical insulation property and accounts for the high electrical breakdown strength at $x = 6$.

Figure 6(a) shows the composition dependence of P–E loops for the as-prepared ceramics, in which all compositions exhibit slim P–E loops. It is interesting that significantly delayed polarization saturation is observed for the high Zr^{4+} doping compositions. To qualitatively evaluate the degree of delayed polarization saturation, the ratio of W_{rec} against the electric field (W_{rec}/E) is calculated and depicted in Fig. 6(b). W_{rec}/E increases with an enhancement of the electric field and quickly reaches a platform with a maximum value of ~8.5 J/(cm²·V) at a critical electric field of around 150 kV/cm. In comparison, the compositions with Zr^{4+} additives exhibit much higher critical electric field and platform value, for example, the composition of $x = 6$ exhibits an obviously increased critical electric field over 200 kV/cm and high maximum W_{rec}/E of 11.8 J/(cm²·V). The improved critical electric field and platform value imply obvious delayed saturation polarization, which makes the materials promising for achieving higher energy storage density. Meanwhile, it should be noted that at lower electric fields, the polarization for the low Zr^{4+} doping compositions is moderately large, of which the increasing rate is limited at higher fields. In other words, the low Zr^{4+} doping compositions possess large polarization nonlinearity. However, for the high Zr^{4+} doping compositions, this effect is weakened. To quantitatively describe the polarization nonlinearity, the tangent dielectric constant change ($\partial P/\partial E$, TPC calculated from the polarization upswing and downswing) of the charge–discharge curve is employed as Eq. (4):

$$\mathrm{TPC} = \frac{\mathrm{TP}(E) - \mathrm{TP}(0)}{\mathrm{TP}(0)} \times 100\% \tag{4}$$

where TP(0) and TP(E) represent the tangent permittivity at the electric field strength of 0 and E, respectively. As exhibited in Fig. 6(c), for the high Zr^{4+} content components, TPC is higher under the same electric field. In other words, for the same value of TPC, the ceramics with the higher Zr^{4+} content require a large applied electric field, which further confirms the conclusion that the polarization nonlinearity (or high polarization saturation field) gradually decreases with the increase of Zr^{4+} [38]. Figure 6(d) shows unipolar P–E loops of all compositions under an electric field prior to respective breakdown strength. Small hysteresis with low P_r is observed in all P–E loops, in accordance with the high RFE feature for all compositions. Based on the P–E loops, W_{rec} and η are calculated and shown in Fig. 6(e). W_{rec} is 4.1 J/cm³ for $x = 0$, which increases with increasing the Zr^{4+} content and reaches a maximum of 6.6 J/cm³ for $x = 6$. However, a further addition of Zr^{4+} reduces the energy storage density. Of particular importance is that all compositions exhibit high η over 90%, especially ultrahigh η of 93.5% achieved for $x = 6$. Furthermore, the P–E loops keep slim under various electric fields for the composition of $x = 6$ (Fig. 6(f)), which leads to a linear increase of the energy storage density and ultrahigh η of beyond 90% with the increase of the electric field (Fig. 6(g)). The above results prove that the strategy of introducing Zr^{4+} to improve the relaxor feature and delay polarization saturation is effective for enhancing W_{rec}. In addition, in comparison with some other state-of-the-art lead-free perovskite bulk ceramics, the NBBSCT-6Z ceramics exhibit an

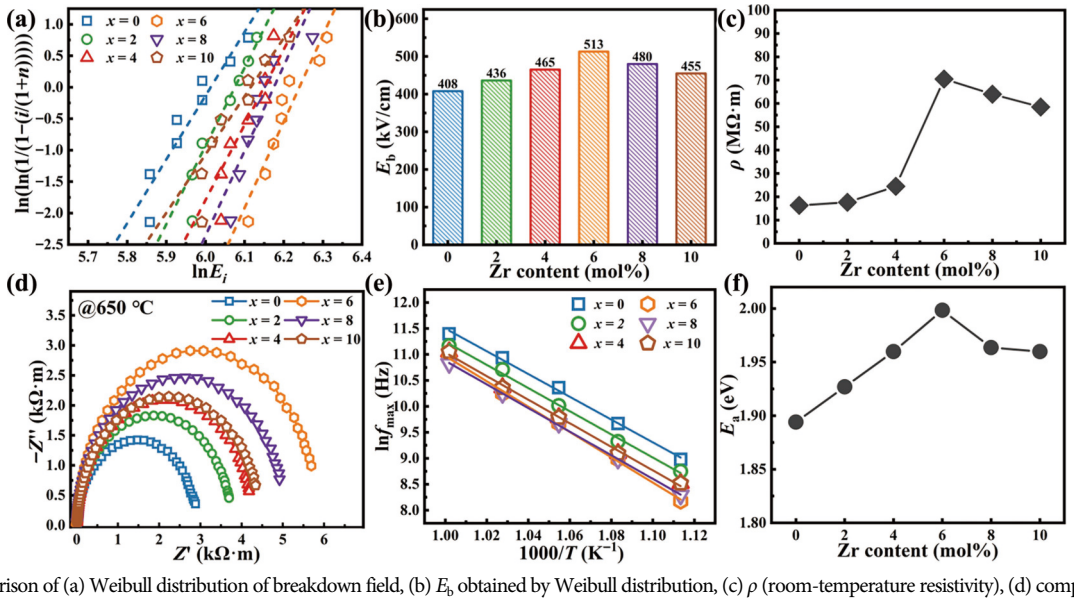

Fig. 5 Comparison of (a) Weibull distribution of breakdown field, (b) E_b obtained by Weibull distribution, (c) ρ (room-temperature resistivity), (d) complex impedance tested under 650 ℃, (e) Arrhenius lines ($\ln f_{max}$ vs. $1000/T$) where f_{max} means the frequency at which the maximum ($-Z''$) value is obtained, and (f) E_a.

obvious advantage in keeping both high η and W_{rec}, as shown in Fig. 6(h). All the above properties indicate it is an attractive candidate for energy storage applications [15,39–48].

From an application perspective, the stability of dielectric materials is also an essential bench index that should be considered. Figure 7(a) shows the frequency dependence of the *P*–*E* loops

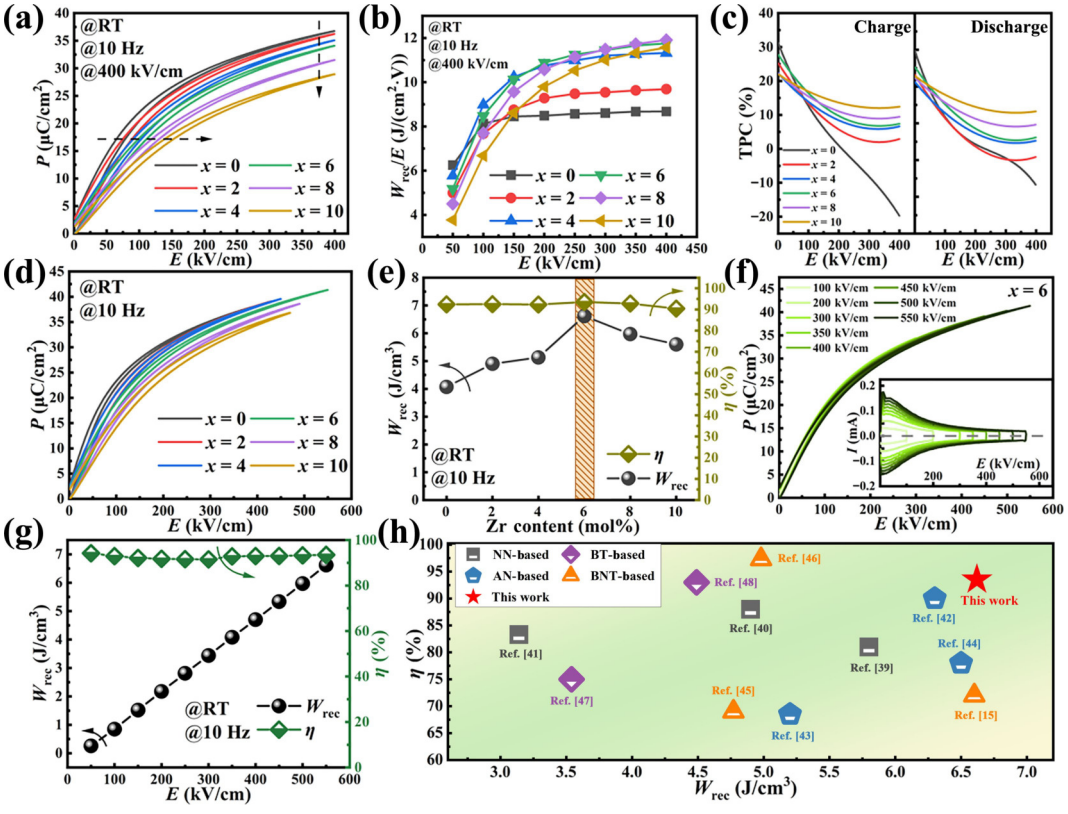

Fig. 6 (a) Unipolar *P*–*E* loops when achieving the same electric field. (b) Electric field dependence of W_{rec}/E for all compositions at the same electric field. (c) Relationship between tangent dielectric constant and external electric field in charge and discharge curves. (d) Unipolar *P*–*E* loops for all compositions measured prior to each breakdown strength. (e) Zr^{4+} content dependence of W_{rec} and η. (f) Electric field dependence of unipolar *P*–*E* loop (the inset gives *I*–*E* curves). (g) Energy storage properties under breakdown strength of NBBSCT-6Z ceramics. (h) Comparison of W_{rec} and η values with some of state-of-the-art lead-free perovskite bulk ceramics.

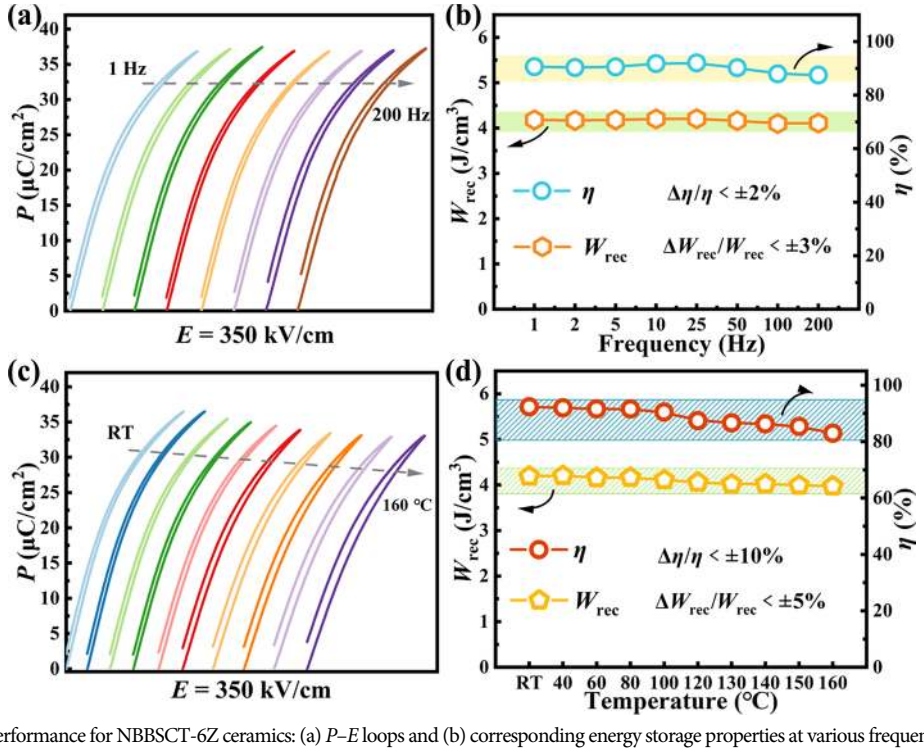

Fig. 7 Energy storage performance for NBBSCT-6Z ceramics: (a) *P*–*E* loops and (b) corresponding energy storage properties at various frequencies under 350 kV/cm at room temperature. (c) *P*–*E* loops and (d) corresponding energy storage properties at various temperatures under 350 kV/cm at fixed frequency of 10 Hz.

under a fixed electric field of 350 kV/cm for the composition of $x = 6$. Over the frequency range from 1 to 200 Hz, the *P*–*E* loops maintain slim with slight fluctuation for P_m and P_r. Thus, W_{rec} keeps very stable in the range of 4.1–4.2 J/cm³ and high η of ~90% (Fig. 7(b)), demonstrating good frequency stability. Meanwhile, energy storage devices often work in extreme and/or high-temperature environments, and the temperature stability is also a pivotal evaluation parameter. Figure 7(c) shows the temperature dependence of the *P*–*E* loops under 350 kV/cm for the composition of $x = 6$, in the temperature range from RT to 160 ℃. Slim *P*–*E* loops are observed at various temperatures, with a small decrease in maximum polarization. It is interesting that W_{rec} keeps very stable around 4.1 J/cm³, showing a minimum variation of less than 5% (Fig. 7(d)), which indicates excellent thermal stability. Besides, even though the energy storage efficiency exhibits a certain reduction due to an enhanced leakage at high temperatures, high η of 83% is still obtained at 160 ℃.

In addition, the charge–discharge performance is also a very important criterion to evaluate the practicability of a capacitor. To evaluate the feasibility of the NBBSCT-6Z ceramics, pulse charge–discharge measurements are conducted under various conditions, as shown in Fig. 8. Figures 8(a) and 8(b) display the overdamped charge–discharge performance for the composition of $x = 6$. The discharge energy density (W_{dis}) increases significantly with the enhancement of the electric field and reaches a maximum of 6.3 J/cm³ is obtained under 500 kV/cm, consistent with the results calculated from the *P*–*E* loops. Moreover, 90% of the stored energy can be released in less than 11 μs ($t_{0.9}$), which shows fast discharge speed. Meanwhile, Figs. 8(c) and 8(d) show the temperature dependence of W_{dis} and $t_{0.9}$ under 350 kV/cm for the composition of $x = 6$ in the temperature range from RT to 160 ℃. W_{dis} stays relatively stable in the range of 3.5–4.1 J/cm³ with a minor variation of 12% when the temperature rises from RT to 160 ℃. Also, $t_{0.9}$ also keeps stable in the range of 6.9–7.9 μs with a minor variation of 10%. The phenomenon indicates good thermal stability.

4 Conclusions

$(Na_{0.2}Bi_{0.2}Ba_{0.2}Sr_{0.2}Ca_{0.2})(Ti_{1-x\%}Zr_{x\%})O_3$ high-entropy relaxor ferroelectric bulk ceramics were prepared. The phase structure, dielectric, and ferroelectric analysis indicated that the addition of Zr^{4+} could drastically tune the relaxor feature, which contributed to delayed polarization saturation. High W_{rec} of 6.6 J/cm³ with ultra-high η of 93.5% was realized in the ceramics of $x = 6$. Meanwhile, the ceramics of $x = 6$ also demonstrated excellent frequency and thermal stability, as well as good charge–discharge performance, which indicates that it is promising for energy storage applications. This work provides an effective strategy to enhance both energy storage density and efficiency of ceramic capacitors.

Appendix

The diffuseness parameter (γ) is fitted by the modified Curie–Weiss law (Eq. (A.1)):

$$1/\varepsilon_r - 1/\varepsilon_m = (T - T_m)^\gamma / C \quad (1 \le \gamma \le 2) \tag{A.1}$$

where ε_m denotes the dielectric maximum and T_m is its temperature. $\gamma = 1$ describes the typical ferroelectric behavior which completely follows Curie–Weiss law, and $\gamma = 2$ represents the ideal relaxor ferroelectric which undergoes a complete diffuse phase transition. The value of γ could reveal the ferroelectric to relaxor behaviour in the respective range of 1–2, and the larger value of γ reflects the better relaxor performance.

Weibull distribution is calculated from Eqs. (A.2.1) and (A.2.2):

$$X_i = \ln E_i \tag{A.2.1}$$

$$Y_i = \ln\left(\ln\left(1\Big/\left(1 - \frac{i}{n+1}\right)\right)\right) \tag{A.2.2}$$

where E_i is the breakdown field of the ith sample arranged in the

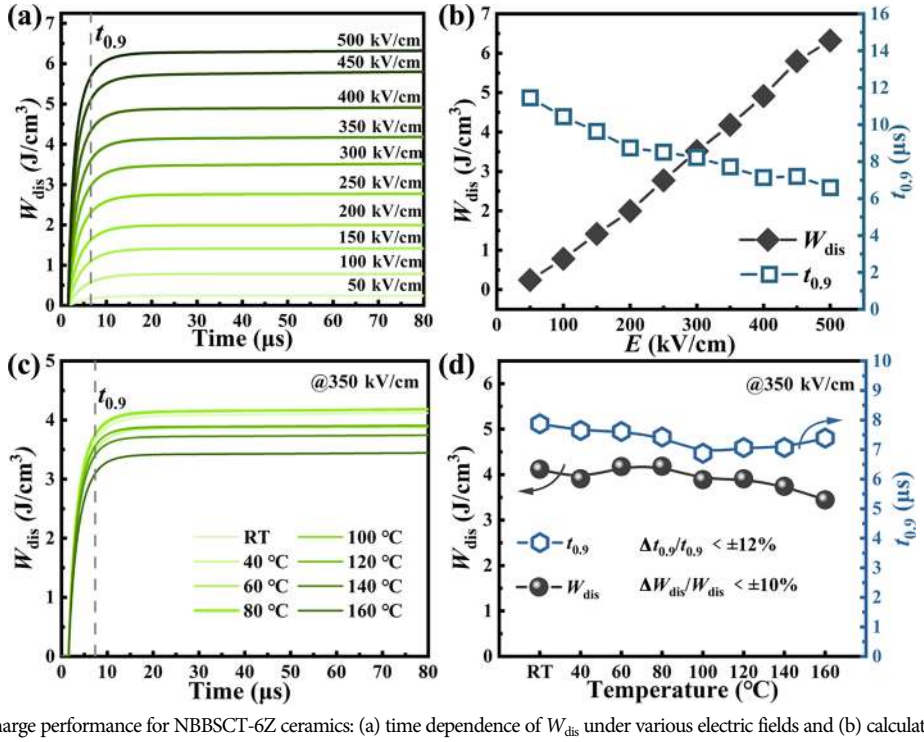

Fig. 8 Charge and discharge performance for NBBSCT-6Z ceramics: (a) time dependence of W_{dis} under various electric fields and (b) calculated W_{dis} and $t_{0.9}$. (c) Time dependence of W_{dis} at different temperatures under 350 kV/cm and (d) as-calculated W_{dis} and $t_{0.9}$ at different temperatures.

ascending order, and n is the total number. A linear relationship will be displayed in X_i and Y_i, with a shape parameter value (β) assessing the fluctuation of the materials' synthetic quality.

Acknowledgements

This work was financially supported by the Guangxi Natural Science Fund for Distinguished Young Scholars (Grant No. 2022GXNSFFA035034), National Natural Science Foundation of China (Grant Nos. 52072080 and U22A20127), and National Key R&D Program of China (Grant No. 2022YFC2408600). We also would like to acknowledge the support from Xiaomi Foundation/Xiaomi Young Talents Program.

Declaration of competing interest

The authors have no competing interests to declare that are relevant to the content of this article.

Electronic Supplementary Material

Supplementary material is available in the online version of this article at https://doi.org/10.26599/JAC.2024.9220859.

References

[1] Palneedi H, Peddigari M, Hwang GT, *et al.* High-performance dielectric ceramic films for energy storage capacitors: Progress and outlook. *Adv Funct Mater* 2018, **28**: 1803665.

[2] Liu Z, Lu T, Ye JM, *et al.* Antiferroelectrics for energy storage applications: A review. *Adv Mater Technol* 2018, **3**: 1800111.

[3] Li JL, Shen ZH, Chen XH, *et al.* Grain-orientation-engineered multilayer ceramic capacitors for energy storage applications. *Nat Mater* 2020, **19**: 999–1005.

[4] Qi H, Zuo RZ, Xie AW, *et al.* Ultrahigh energy-storage density in $NaNbO_3$-based lead-free relaxor antiferroelectric ceramics with nanoscale domains. *Adv Funct Mater* 2019, **29**: 1903877.

[5] Yan F, He X, Bai HR, *et al.* Excellent energy storage properties and superior stability achieved in lead-free ceramics via a spatial sandwich structure design strategy. *J Mater Chem A* 2021, **9**: 15827–15835.

[6] Yang LT, Kong X, Li F, *et al.* Perovskite lead-free dielectrics for energy storage applications. *Prog Mater Sci* 2019, **102**: 72–108.

[7] Zhou XF, Qi H, Yan ZN, *et al.* Superior thermal stability of high energy density and power density in domain-engineered $Bi_{0.5}Na_{0.5}TiO_3$–$NaTaO_3$ relaxor ferroelectrics. *ACS Appl Mater Interfaces* 2019, **11**: 43107–43115.

[8] Ye HR, Yang F, Pan ZB, *et al.* Significantly improvement of comprehensive energy storage performances with lead-free relaxor ferroelectric ceramics for high-temperature capacitors applications. *Acta Mater* 2021, **203**: 116484.

[9] Petzelt J, Kamba S, Fábry J, *et al.* Infrared, Raman and high-frequency dielectric spectroscopy and the phase transitions in $Na_{1/2}Bi_{1/2}TiO_3$. *J Phys Condens Mat* 2004, **16**: 2719–2731.

[10] Levin I, Reaney IM. Nano- and mesoscale structure of $Na_{1/2}Bi_{1/2}TiO_3$: A TEM perspective. *Adv Funct Mater* 2012, **22**: 3445–3452.

[11] Xu KL, Yang P, Peng W, *et al.* Temperature-stable MgO-doped BCZT lead-free ceramics with ultra-high energy storage efficiency. *J Alloys Compd* 2020, **829**: 154516.

[12] Wang T, Jin L, Li CC, *et al.* Relaxor ferroelectric $BaTiO_3$–$Bi(Mg_{2/3}Nb_{1/3})O_3$ ceramics for energy storage application. *J Am Ceram Soc* 2015, **98**: 559–566.

[13] Chu BK, Hao JG, Li P, *et al.* High-energy storage properties over a broad temperature range in La-modified BNT-based lead-free ceramics. *ACS Appl Mater Interfaces* 2022, **14**: 19683–19696.

[14] Yan F, Huang KW, Jiang T, *et al.* Significantly enhanced energy storage density and efficiency of BNT-based perovskite ceramics via A-site defect engineering. *Energy Storage Mater* 2020, **30**: 392–400.

[15] Che ZY, Ma L, Luo GG, *et al.* Phase structure and defect engineering in $(Bi_{0.5}Na_{0.5})TiO_3$-based relaxor antiferroelectrics toward excellent energy storage performance. *Nano Energy* 2022, **100**: 107484.

[16] Qi H, Zuo RZ. Giant electrostrictive strain in $(Bi_{0.5}Na_{0.5})TiO_3$–$NaNbO_3$ lead-free relaxor antiferroelectrics featuring temperature and frequency stability. *J Mater Chem A* 2020, **8**: 2369–2375.

[17] Guo S, Liu CT. Phase stability in high entropy alloys: Formation of solid-solution phase or amorphous phase. *Prog Nat Sci Mater Int* 2011, **21**: 433–446.

[18] Anand G, Wynn AP, Handley CM, *et al.* Phase stability and distortion in high-entropy oxides. *Acta Mater* 2018, **146**: 119–125.

[19] Yeh JW, Chen SK, Lin SJ, *et al.* Nanostructured high-entropy alloys with multiple principal elements: Novel alloy design concepts and outcomes. *Adv Eng Mater* 2004, **6**: 299–303.

[20] Rost CM, Sachet E, Borman T, *et al.* Entropy-stabilized oxides. *Nat Commun* 2015, **6**: 8485.

[21] Xiang HM, Xing Y, Dai FZ, *et al.* High-entropy ceramics: Present status, challenges, and a look forward. *J Adv Ceram* 2021, **10**: 385–441.

[22] Ji HF, Wang DW, Bao WC, *et al.* Ultrahigh energy density in short-range tilted NBT-based lead-free multilayer ceramic capacitors by nanodomain percolation. *Energy Storage Mater* 2021, **38**: 113–120.

[23] Chen L, Deng SQ, Liu H, *et al.* Giant energy-storage density with ultrahigh efficiency in lead-free relaxors via high-entropy design. *Nat Commun* 2022, **13**: 3089.

[24] Yang BB, Zhang QH, Huang HB, *et al.* Engineering relaxors by entropy for high energy storage performance. *Nat Energy* 2023, **8**: 956–964.

[25] Pu YP, Zhang QW, Li R, *et al.* Dielectric properties and electrocaloric effect of high-entropy $(Na_{0.2}Bi_{0.2}Ba_{0.2}Sr_{0.2}Ca_{0.2})TiO_3$ ceramic. *Appl Phys Lett* 2019, **115**: 223901.

[26] Zhu XP, Gao YF, Shi P, *et al.* Ultrahigh energy storage density in $(Bi_{0.5}Na_{0.5})_{0.65}Sr_{0.35}TiO_3$-based lead-free relaxor ceramics with excellent temperature stability. *Nano Energy* 2022, **98**: 107276.

[27] Akram F, Sheeraz M, Hussain A, *et al.* Thermally-stable high energy-storage performance over a wide temperature range in relaxor-ferroelectric $Bi_{1/2}Na_{1/2}TiO_3$-based ceramics. *Ceram Int* 2021, **47**: 23488–23496.

[28] Sun NN, Li Y, Zhang QW, *et al.* Giant energy-storage density and high efficiency achieved in $(Bi_{0.5}Na_{0.5})TiO_3$–$Bi(Ni_{0.5}Zr_{0.5})O_3$ thick films with polar nanoregions. *J Mater Chem C* 2018, **6**: 10693–10703.

[29] Shannon RD, Fischer RX. Empirical electronic polarizabilities in oxides, hydroxides, oxyfluorides, and oxychlorides. *Phys Rev B* 2006, **73**: 235111.

[30] Tang XG, Chew KH, Chan HLW. Diffuse phase transition and dielectric tunability of $Ba(Zr_yTi_{1-y})O_3$ relaxor ferroelectric ceramics. *Acta Mater* 2004, **52**: 5177–5183.

[31] Yu Z, Ang C, Guo RY, *et al.* Ferroelectric-relaxor behavior of $Ba(Ti_{0.7}Zr_{0.3})O_3$ ceramics. *J Appl Phys* 2002, **92**: 2655–2657.

[32] Zhao CL, Yang JL, Huang YL, *et al.* Broad-temperature-span and large electrocaloric effect in lead-free ceramics utilizing successive and metastable phase transitions. *J Mater Chem A* 2019, **7**: 25526–25536.

[33] Lei C, Bokov AA, Ye ZG. Ferroelectric to relaxor crossover and dielectric phase diagram in the $BaTiO_3$–$BaSnO_3$ system. *J Appl Phys* 2007, **101**: 084105.

[34] Wang G, Lu ZL, Li Y, *et al.* Electroceramics for high-energy density capacitors: Current status and future perspectives. *Chem Rev* 2021, **121**: 6124–6172.

[35] Tian CY, Wang FF, Ye X, *et al.* Bipolar fatigue-resistant behavior in ternary $Bi_{0.5}Na_{0.5}TiO_3$–$BaTiO_3$–$SrTiO_3$ solid solutions. *Scripta Mater* 2014, **83**: 25–28.

[36] Steinsvik S, Bugge R, Gjønnes J, *et al.* The defect structufe of $SrTi_{1-x}Fe_xO_{3-y}$ (x = 0–0.8) investigated by electrical conductivity measurements and electron energy loss spectroscopy (EELS). *J Phys Chem Solids* 1997, **58**: 969–976.

[37] Zhao XY, Bai WF, Ding YQ, *et al.* Tailoring high energy density with superior stability under low electric field in novel $(Bi_{0.5}Na_{0.5})TiO_3$-

based relaxor ferroelectric ceramics. *J Eur Ceram Soc* 2020, **40**: 4475–4486.

[38] Li X, Cheng Y, Wang F, *et al.* Enhancement of energy storage and hardness of $(Na_{0.5}Bi_{0.5})_{0.7}Sr_{0.3}TiO_3$-based relaxor ferroelectrics via introducing $Ba(Mg_{1/3}Nb_{2/3})O_3$. *Chem Eng J* 2022, **431**: 133441.

[39] Luo GG, Zhuang DY, Yang KH, *et al.* Enhanced comprehensive energy storage properties in $NaNbO_3$-based relaxor antiferroelectric via MnO_2 modification. *J Mater Sci Mater Electron* 2023, **34**: 1444.

[40] Yang LT, Kong X, Cheng ZX, *et al.* Enhanced energy storage performance of sodium niobate-based relaxor dielectrics by a ramp-to-spike sintering profile. *ACS Appl Mater Interfaces* 2020, **12**: 32834–32841.

[41] Dong XY, Li X, Chen HY, *et al.* Realizing enhanced energy storage and hardness performances in $0.90NaNbO_3$–$0.10Bi(Zn_{0.5}Sn_{0.5})O_3$ ceramics. *J Adv Ceram* 2022, **11**: 729–741.

[42] Luo NN, Han K, Cabral MJ, *et al.* Constructing phase boundary in $AgNbO_3$ antiferroelectrics: Pathway simultaneously achieving high energy density and efficiency. *Nat Commun* 2020, **11**: 4824.

[43] Luo NN, Han K, Zhuo FP, *et al.* Aliovalent A-site engineered $AgNbO_3$ lead-free antiferroelectric ceramics toward superior energy storage density. *J Mater Chem A* 2019, **7**: 14118–14128.

[44] Ma L, Che ZY, Xu C, *et al.* High energy storage density and efficiency in $AgNbO_3$ based relaxor antiferroelectrics with reduced silver content. *J Eur Ceram Soc* 2023, **43**: 3228–3235.

[45] Bian SS, Yue ZX, Shi YZ, *et al.* Ultrahigh energy storage density and charge–discharge performance in novel sodium bismuth titanate-based ceramics. *J Am Ceram Soc* 2020, **104**: 936–947.

[46] Zhang LY, Zhang AM, Hou HP, *et al.* Stronger B-site ionic disorder boosting enhanced dielectric energy-storage performance in BNT-based relaxor ferroelectric ceramics. *Ceram Int* 2023, **49**: 7905–7912.

[47] Liu G, Li Y, Guo B, *et al.* Ultrahigh dielectric breakdown strength and excellent energy storage performance in lead-free barium titanate-based relaxor ferroelectric ceramics via a combined strategy of composition modification, viscous polymer processing, and liquid-phase sintering. *Chem Eng J* 2020, **398**: 125625.

[48] Hu Q, Tian Y, Zhu QS, *et al.* Achieve ultrahigh energy storage performance in $BaTiO_3$–$Bi(Mg_{1/2}Ti_{1/2})O_3$ relaxor ferroelectric ceramics via nano-scale polarization mismatch and reconstruction. *Nano Energy* 2020, **67**: 104264.